Ng, C. W. W. *et al. Géotechnique* [http://dx.doi.org/10.1680/jgeot.16.P.273]

Dry granular flow interaction with dual-barrier systems

C. W. W. NG*, C. E. CHOI†, R. C. H. KOO‡, G. R. GOODWIN*, D. SONG* and J. S. H. KWAN‡

Multiple barriers are commonly installed along predicted geophysical flow paths to intercept large flow volumes. The main criterion for multiple-barrier design is volume retained. The velocity of the incoming (far-field) undisturbed flow is also sometimes used, although this neglects the influence of other obstacles on the flow characteristics. This study investigates the influence of upstream flow–barrier interaction on downstream runup and impact mechanisms of a dual rigid barrier system. Four physical flume tests were performed using dry sand to investigate flow interaction with dual barriers. Moreover, three-dimensional finite-element simulations were conducted to back-analyse the flume tests and to investigate the effects of upstream barrier height and barrier spacing on downstream impact characteristics. Two key interaction mechanisms that alter downstream flow are identified: (*a*) flow momentum redirection (i.e. runup) at the upstream barrier, reducing pre-impact momentum at the downstream; and (*b*) downstream flow-thinning. Runup mechanisms at the upstream barrier and flow-thinning between the two successive barriers have profound effects on dynamic impact pressures at the downstream barrier. When the upstream barrier height is taller than twice the maximum flow thickness, flow energy can be dissipated effectively by momentum redirection. The downstream barrier height and design impact pressure can be reduced up to 17% and 35% for dry sand flows, respectively.

KEYWORDS: landslides; slopes; soil/structure interaction

INTRODUCTION

Barriers are placed in natural channels to arrest geophysical flows. For large design flow volumes, multiple-barrier systems (Glassey, 2013) are usually installed to progressively retain flow material (WSL, 2008; Shum & Lam, 2011). Advantageously, individual barrier design within a multi-barrier system may be varied, thus flexibly coping with site constraints and minimising flow acceleration along natural channels (Wong, 2009). Existing international guidelines for the design of multiple-barrier systems mainly consider the volume retained (CGS, 2004; NILIM, 2007; Kwan, 2012; Kwan *et al*., 2015), but neglect flow–barrier interaction that can change the downstream flow Froude conditions. This is potentially catastrophic: Wang (2013) describes failure of prescriptively installed multiple-barrier systems impacted by debris flows in 2010 in Zhouqu, China. Scientific investigation of such flow–barrier interaction scenarios is thus clearly warranted.

Interaction between dry granular flows and a single obstacle has been investigated, revealing key impact mechanisms, such as dead-zone development (Faug *et al*., 2002; Gray *et al*., 2003), runup (Mancarella & Hungr, 2010; Choi *et al*., 2015) and overflow (Hákonardóttir *et al*., 2003a, 2003b; Choi *et al*., 2014a). Analytic solutions have also been proposed: for example, Faug (2015a) conducted a series of small-scale experiments using dry sand flow impacting obstacles along an incline. A depth-averaged analytic solution describing the impact dynamics was proposed. It was revealed that various granular phenomena resulting from flow–wall interaction significantly influence the interaction between dry sand flows and protection structures.

By contrast, few studies consider flow–structure interaction for multiple rows of structural countermeasures. Choi *et al*. (2014a) and Ng *et al*. (2014) studied the influence of multiple rows of baffles on dry granular flow, finding that structure spacing partially governs downstream flow dynamics. Hákonardóttir *et al*. (2003a) carried out a series of scaled laboratory experiments using glass particles with a mean diameter of 100 μm to investigate the interaction between supercritical flows and mounds. It was found that the mounds cause a significant dissipation of the kinetic energy of the flow. This implies that the dissipation of landing energy should be an important consideration for dual-barrier systems. Furthermore, Naaim *et al*. (2010) employed numerical modelling and statistical analysis to back-analyse dense-flow avalanches in Taconnaz on existing passive structures. Key findings reveal that the avalanche volume and the Froude number are two key variables for characterising the interaction between avalanches and obstacles. However, the structures investigated in these studies are fundamentally different from rigid barriers, as they are not designed for debris retention.

Kwan *et al*. (2015) proposed a relationship for calculating multiple-barrier spacing based on a point mass trajectory theory using conservation of energy. The overflow trajectory is assumed to be dependent on the barrier height, flow thickness, slope channel inclination and overflow Froude conditions. It is assumed that there is no air entrainment and no change of density during the overflow process. The overflow length x_i from the upstream barrier is calculated using

$$x_i = h\mathrm{Fr}^2\left(\tan\theta + \sqrt{\tan^2\theta + \frac{2B}{h\mathrm{Fr}^2}}\right) \quad (1)$$

Manuscript received 24 October 2016; revised manuscript accepted 26 June 2017.
Discussion on this paper is welcomed by the editor.
* Department of Civil and Environmental Engineering, Hong Kong University of Science and Technology, Clear Water Bay, Kowloon, Hong Kong.
† Department of Civil and Environmental Engineering, and Institute for Advanced Study, Hong Kong University of Science and Technology, Clear Water Bay, Kowloon, Hong Kong.
‡ Geotechnical Engineering Office, Civil Engineering and Development Department, Hong Kong SAR Government.

where h is upstream flow thickness, Fr is the Froude number, θ is channel inclination and B is barrier height. The Froude number is defined as follows

$$\mathrm{Fr} = \frac{v}{\sqrt{gh\cos\theta}} \tag{2}$$

where v is the pre-impact velocity; g is acceleration due to gravity; h is the pre-impact flow thickness; and θ is the channel inclination. Although equation (1) suggests a minimum spacing for multiple barriers, neither downstream Froude conditions nor key impact characteristics at the downstream barrier can be calculated, as with the volume-based approach.

The focus of this study is on the interaction between dry sand flows and dual barriers. It should be noted that findings may be directly applicable to dry granular flows observed in nature such as debris avalanches, but cannot be assumed to be applicable to debris flows where both the solid and fluid phases vitally influence the flow dynamics (Iverson, 1997). Although dry sand flows cannot represent all types of geophysical flows, they are simple and thus suitable for bench-marking the proposed framework in this study. Physical test data were then back-analysed using a three-dimensional finite-element model. A parametric study was performed to investigate the effects of upstream barrier height and spacing between barriers on downstream Froude conditions, and hence runup height and impact pressure.

SCALING AND FLOW CHARACTERISATION

Geometric and dynamic similitude between model and prototype flows is crucial for meaningful flume tests (Iverson, 2015). Both open-channel flows and flow–structure interaction are driven by inertial and gravitational forces. The Froude number characterises the relative importance of each of these forces, and so is vital for scaling flow–structure interaction (Armanini *et al*., 2011, 2014; Armanini, 2015); a Froude number of unity indicates equal importance. Faug (2015a) presents findings related to flow–wall interaction, including dimensionless parameters and a phase diagram for granular flow–wall interaction considering various Froude conditions. Faug (2015a) characterises the different zones of the phase diagram into steady airborne jets, a standing granular jump, a dead zone and unsteady bore based on Fr and height of obstacle. In this study, the range of impacting Froude conditions and barrier height is within the transition zone between the regime of granular jumps ($1{\cdot}0 < \mathrm{Fr} \leq 4{\cdot}0$) and the formation of granular dead zones ($\mathrm{Fr} \leq 1{\cdot}0$). This means that the granular jumps and dead zones are important flow mechanisms. Both Hübl *et al*. (2009) and Cui *et al*. (2015) reported that, for natural geophysical flows, Fr is less than five; this range is targeted in this study.

Flows may be classified as dilute or dense, depending on the solid volume fraction. For dilute flows, compressibility, and hence dilatancy, become important. Faug *et al*. (2015) reports that a compressible granular jump occurs when the flows moves from a dense to a dilute regime during overflow. This produces a transition between incompressible and compressible conditions. Faug (2015a) further demonstrated that the observed jump height decreases for dilute flows due to dispersal of overflow particles. For such cases, interpreting results based on a macroscopic approach without consideration of these two phenomena may be inappropriate. For dense flows, Bryant *et al*. (2015) reports that stress-dilatancy may safely be ignored. In the present study, the majority of the processes observed constitute dense granular flows, for which stress-dilatancy may be neglected. Only the overflow processes involved move into the dilute regime for which compressibility is important, explaining the differences observed between physical and computed data.

IMPACT PRESSURE CALCULATION

The hydrodynamic approach is commonly adopted to estimate the impact pressure for a single barrier (Jóhannesson *et al*., 2009; Kwan, 2012). This approach assumes that the impact pressure is proportional to the square of the flow velocity. An empirical coefficient α absorbs terms relating to gravitational forces

$$P = \alpha\rho v^2 \tag{3}$$

For rigid barrier design, Jóhannesson *et al*. (2009) recommends an α value of 1·0, accounting for a non-uniform velocity profile derived from the principle of conservation of momentum, whereas Kwan (2012) suggests an α value of 2·5 for design purposes, considering potential discrete large impacts due to hard inclusions. Cui *et al*. (2015) proposed an empirical relationship between α and the Froude number based on extensive field analyses, specifically a relationship of $\alpha = 5{\cdot}3\mathrm{Fr}^{-1{\cdot}5}$. The impact models proposed by Kwan (2012) and Cui *et al*. (2015) conservatively assume that the impact pressure along the height of the barrier is constant and equal to the maximum pressure at the base.

Faug (2015b) investigated the force induced by granular flows on obstacles for a wide range of Froude conditions. He showed that the measured average force increases linearly with the square of the mean velocity of the undisturbed granular flow in the rapid regime, regardless of whether it is dense or dilute.

Other studies specifically related to snow avalanches have been carried out to investigate the correlation between α and Fr based on measured data from field and laboratory tests (Gauer *et al*., 2007a, 2007b; Thibert *et al*., 2013; Sovilla *et al*., 2016). These studies also suggest that α is proportional to the inverse square of Fr. Sovilla *et al*. (2016) specifically recommended that for Fr larger than unity, both the static force due to gravity and dynamic force in terms of square of impact flow velocity should be considered. Thibert *et al*. (2013) studied a full-scale snow avalanche test site in the southern French Alps. Findings revealed that α for an avalanche on an obstacle is a function of the velocity and is inversely proportional to the Froude conditions.

FLUME MODELLING

A 5 m long inclinable rectangular flume model (Choi *et al*., 2014a) was used to study the flow–structure impact mechanisms for a dual-barrier system. The flume is 500 mm deep and 200 mm wide. A hopper with a storage volume of 0·06 m^3 retains material. A remote-controlled gate facilitates dam-break.

Instrumentation

Figure 1 shows a schematic representation of the side view of the flume model and instrumentation. Flow kinematics were captured using high-speed cameras facing the channel walls. The cameras use a resolution of 1312×556 pixels and a frame rate of 200 frames/s, with 1000 W lamps providing the illumination. It is acknowledged that shearing effects exist along the boundaries of the channel, so the flow kinematics captured using the high-speed camera at the side wall differ slightly from that at the centreline of the channel. The channel in this study has a width of 0·2 m and the maximum particle diameter is 0·6 mm. Jop *et al*. (2006) reported that the flow velocity depends primarily on particle

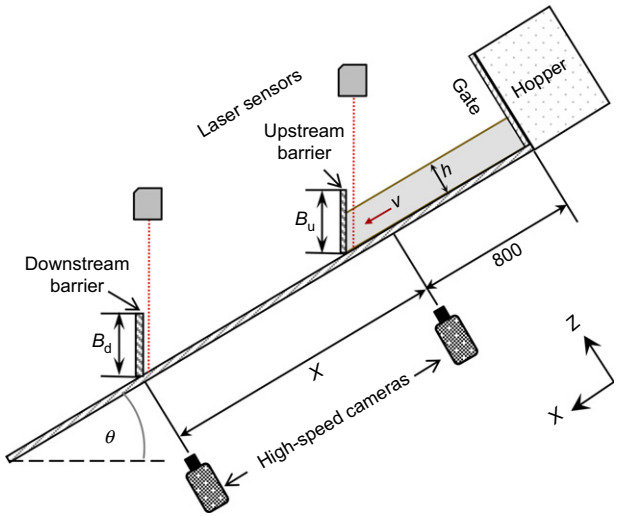

Fig. 1. Schematic diagram giving side view of the physical flume model set-up (dimensions in mm)

diameter and shear rate when the ratio between the particle size and channel width is more than ten. The effect of arching in this study should thus be relatively small, minimising boundary effects that may influence data from high-speed videography.

Laser displacement sensors (Wenglor YT44MGV80) captured the flow thickness profile directly upstream of both barriers. These laser sensors were installed along the centreline above the channel to measure the change of flow thickness (Fig. 2). The flow depth profiles measured using the laser sensors were used to calibrate the numerical model. From the calibrated numerical model, a more comprehensive understanding of the flow behaviour across the channel width can be obtained.

Flume test programme

A reference open-channel control test (test ID: FF) was performed to characterise flow Fr conditions. A further three flume tests investigating a flow–structure impact for a dual-barrier system were conducted (Table 1). In all tests, the channel inclination was 26° to develop flows with a pre-impact Fr of around 3·5, within the range of typical debris flows (Hübl *et al.*, 2009; Cui *et al.*, 2015). Several studies (Faug *et al.*, 2003, 2004, 2008; Hákonardóttir *et al.*, 2003a; Faug, 2015a) indicate that the ratio between flow thickness and barrier height is vital for flow–structure interaction, so three ratios were studied: $B/h_0 = 1{\cdot}1$ ($B = 0{\cdot}1$ m), $B/h_0 = 2{\cdot}0$ ($B = 0{\cdot}18$ m), and $B/h_0 = 2{\cdot}9$ ($B = 0{\cdot}26$ m), where h_0 is the observed maximum flow thickness measured in the open-channel control test (0·09 m).

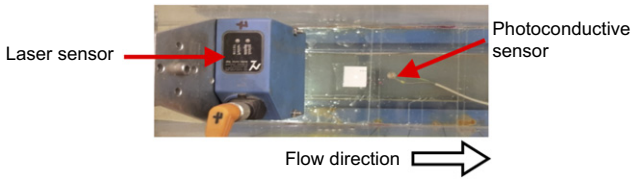

Fig. 2. Laser sensors on the flume (top-down view)

Table 1. Physical flume tests

Test ID	Barrier spacing, L: mm	Upstream barrier height, B: mm
FF	—	—
PX6-B260	700	260
PX6-B180	700	180
PX6-B100	700	100

Testing procedures

Dry Leighton Buzzard (LB) fraction C sand, with a particle diameter of 0·3–0·6 mm, was used. The sand has an internal friction angle of 30·0° and an interface friction angle of 22·6°, determined using the method described in Pudasaini & Hutter (2007).

One hundred kilogrammes of dry sand was placed in the hopper with a bulk density of about 1680 kg/m^3. The flume was inclined, and the gate opened, simulating dam-break (cf. Choi *et al.*, 2014a).

FINITE-ELEMENT MODELLING

LS-Dyna is a three-dimensional large-deformation finite-element method software package, and is used to numerically back-analyse the physical flume tests. The software provides a continuum-based numerical solution, considering energy conservation and Newton's laws of motion.

The arbitrary Lagrangian–Eulerian (ALE) formulation is used to model granular flow material during large deformations. The computational domain is discretised into a mesh of hexahedral elements, which can move arbitrarily. The elements record the acceleration, velocity, displacement, strain, stress and kinetic energy of the flow mass within the computational domain.

The finite-element method used in LS-Dyna can also explicitly simulate internal shearing of granular material. The governing equations for internal shearing are based on the Cauchy momentum equations (Hallquist, 2006; Bazilevs *et al.*, 2008)

$$\boldsymbol{\sigma}_{ij} + \rho \boldsymbol{g} = \rho\, \ddot{x} \tag{4}$$

where $\boldsymbol{\sigma}_{ij}$ is the Cauchy stress tensor, ρ is the flow density, $\boldsymbol{g}$ is the body force density (in this case, gravitational acceleration) and $\ddot{x}$ is the acceleration. If the traction boundary conditions are satisfied, equation (4) becomes

$$\boldsymbol{T}_j^{(n)} = \boldsymbol{\sigma}_{ij} \boldsymbol{n}_i \tag{5}$$

where $\boldsymbol{n}$ is a unit vector pointing outwards, normal to a boundary element and $\boldsymbol{T}$ is a stress vector.

The granular material was modelled as elasto-plastic using the Drucker–Prager yield criterion (Drucker & Prager, 1952) following the work of Crosta *et al.* (2003). This approach is widely accepted because the required parameters are available from conventional laboratory testing (Crosta *et al.*, 2003).

With regard to the friction angle: Pouliquen (1999) proposed new scaling laws for granular flows moving down rough inclined planes using small-scale experiments. He found that shear rate dependency and the minimum thickness ratio to the flow thickness varies linearly with Froude number. GDR MiDi (2004) subsequently described the behaviour of dense assemblies of dry grains subjected to continuous shear deformation. This study demonstrates that the flow inertia can be represented by a dimensionless inertial number, I. This number I is equivalent to the square root of Savage number, and as such is shear rate dependent. Crucially, by contrast to 'traditional' implements of the

Savage number, the effective friction coefficient is a function of flow velocity.

Furthermore, Forterre & Pouliquen (2008) conducted dimensional analysis to identify the relation between stresses and shear rates, which was subsequently supported by results from experiments and simulations. Sheared granular flows exhibit shear rate dependence, analogous to a non-Newtonian fluid, leading in turn to a non-uniform friction angle throughout the body. Although evidence exists showing that a constant friction angle is not adequate to model the flow behaviour, a general theoretical correlation between dynamic friction angle and shear rate is still lacking. Given the challenge of obtaining a clear relationship between these two, for the numerical back-analyses presented in this study, a constant equivalent effective friction angle was assumed.

Coulomb's friction law was used to calculate the interface shear resistance (S) between the soil material and the channel surface: $S = N \tan \phi_b$, where N is the normal force and ϕ_b is the basal friction angle.

Interaction between the dry granular material (ALE-based solid elements) and the rigid barrier and channel (shell elements) is modelled using finite-element contacts. Independent motion of contacting elements is calculated over a time step on the order of microseconds (Olovsson & Souli, 2000; Hallquist, 2006). Any penetration of the flow material into the barrier or channel base causes a normal interface reaction force which is distributed evenly to both the flow and the barrier or channel base. The force magnitude is proportional to the penetration and is calculated using an interface spring stiffness governed by the Young's moduli of the flow and shell.

Hungr & Morgenstern (1984) found that the internal friction angle of various granular materials shows no systematic dependence on the shear strain rate. Furthermore, Bryant *et al.* (2015) suggested that a single set of static frictional parameters was broadly suitable for a given material and interface regardless of configuration, validating the use of static friction parameters. The Young's modulus and Poisson ratio are set based on the recommended back-analysed input parameters observed from the field data of frictional flows by Crosta *et al.* (2003) and Kwan *et al.* (2015). These parameters are relevant to elastic deformation and are thus not expected to make a large difference to the flow kinematics, which is undergoing continuous plastic deformation.

Numerical model and simulation procedures

Table 2 shows the input parameters for the numerical analysis. The numerical model set-up is shown in Fig. 3.

Table 2. Input parameters for numerical analysis

Material property	Model parameters
Soil (dry sand)	
Internal friction angle of sand, ϕ: degrees	30·0
Basal friction angle ϕ_b: degrees	22·6
Bulk density, ρ: kg/m^3	1680
Volume of sand used, V: m^3	0·06
Young's modulus, E: MPa	10
Shear modulus, G: MPa	5
Poisson ratio, ν	0·25
Barrier (aluminium)	
Material density, ρ_m: kg/m^3	2700
Young's modulus, E: MPa	69 000
Yield strength: MPa	95
Poisson ratio, ν	0·25

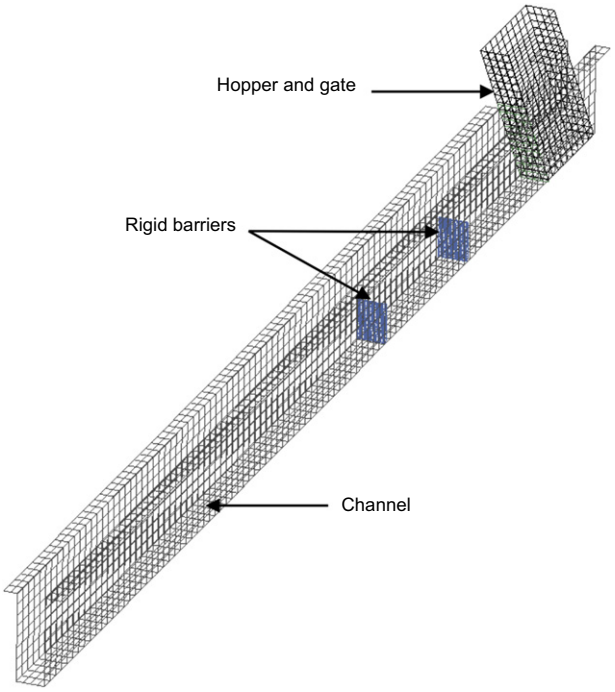

Fig. 3. Numerical model showing hopper, channel, gate and rigid barriers

The physical and numerical flume models are geometrically identical. The storage container, channel base and walls, as well as the rigid barriers were modelled using planar walls. Sand was modelled using elements with 20 mm long sides.

In each simulation, sand was generated within the hopper, and the direction of gravity was altered to simulate inclining the flume. The dry sand is modelled as a quadrilateral solid finite element in the numerical simulations. Once the ALE sand mass reached equilibrium, the gate was deleted to simulate dam-break, allowing material to flow downstream.

Numerical simulation plan

The calibrated numerical model was first used to back-analyse physical flume experiments, followed by a parametric study using the calibrated numerical model. Three spacing ratios between barrier height and flow thickness were studied: $B/h_0 = 1{\cdot}1$ ($B = 100$ mm), $B/h_0 = 2{\cdot}0$ ($B = 180$ mm) and $B/h_0 = 2{\cdot}5$ ($B = 220$ mm). The maximum height of the barrier is reduced to B/h_0 of 2·5 from 2·9 in the computation to allow for overflow. The ratio between barrier spacing and upstream flow thickness approximates the range of that typically used for existing multiple-barrier systems, based on calculations from the retention volume with deposition angle behind the barrier between 10° and 20° (CGS, 2004; NILIM, 2007). The spacing ratio in the field generally lies between 2 and 15, and is adopted in this study. Fig. 1 shows the geometric variables investigated in this study; Table 3 summarises the numerical simulation plan.

INTERPRETATION OF RESULTS

Multiple-barrier impact mechanisms

Figure 4 shows a comparison of (*a*) the observed kinematics; (*b*) velocity fields analysed using particle image velocimetry (PIV) (White *et al.*, 2003); and (*c*) computed impact kinematics for an upstream barrier with a normalised height of $B/h_0 = 2{\cdot}5$ (test ID: PX6-B260). Each frame shows the maximum velocity at that instant. Time $t = 0{\cdot}15$ s

Table 3. Numerical simulation plan

Test ID	Barrier spacing, L: mm	Upstream barrier height, B: mm
L4-B10	400	100
L5-B10	500	
L6-B10	600	
L7-B10	700	
L8-B10	800	
L10-B10	1000	
L15-B10	1500	
L4-B18	400	180
L5-B18	500	
L6-B18	600	
L7-B18	700	
L8-B18	800	
L10-B18	1000	
L15-B18	1500	
L4-B22	400	220
L5-B22	500	
L6-B22	600	
L7-B22	700	
L8-B22	800	
L10-B22	1000	
L15-B22	1500	

(Fig. 4(a)) shows a wedge-like flow front approaching the upstream barrier with a measured velocity of about 2·7 m/s. At time $t = 0{\cdot}19$ s (Fig. 4(b)), sand begins to deposit, forming a dead zone (Faug *et al*., 2002; Gray *et al*., 2003; Ashwood & Hungr, 2016) near the base of the barrier. Subsequent flow impacts the wedge-like dead zone, beginning to run up along the face of the barrier. At time $t = 0{\cdot}27$ s (Fig. 4(c)), the dead zone progressively increases in size, with sand coming to rest in layers.

A gradual change in impact direction from a slope-parallel to a vertical direction can be observed from the evolution of the PIV vectors (Figs 4(a)–4(c)). The numerical model captures the observed frontal velocity and thickness from the flume experiments. The change in impact direction also demonstrates that the ramp-like dead zone formation facilitates the runup mechanism. The numerical simulations reproduce the maximum dead zone height but do not capture the overall length of the physical dead zone well. This is because the numerical model does not consider particle rearrangement or density change: in physical tests, particles tend to pack together efficiently, increasing frictional contact area and tending to retard the flow (Zhou *et al*., 2016). In addition, the numerical model assumes constant basal friction, whereas in reality the basal friction coefficient is rate dependent (Pouliquen, 1999; GDR MiDi, 2004; Forterre & Pouliquen, 2008). Therefore, a larger dead zone can be seen in the physical tests compared to the numerical simulation. This can be corroborated using results presented in Faug *et al*. (2004) and Forterre & Pouliquen (2008), wherein laboratory tests were performed using granular flows down rough inclines to demonstrate the appropriateness of a variable friction model. However, given the lack of a general theoretical relationship between variable friction and other flow parameters, a constant friction angle was adopted in this study.

Figure 5 shows a comparison of the observed and computed overflow kinematics from the upstream barrier (test ID: PX6-B180). The downstream barrier is positioned at a slope-parallel distance of 600 mm from the upstream barrier and has a normalised barrier height of $B/h_0 = 2{\cdot}0$. The downstream barrier is tall enough to prevent overflow so as to fairly compare all downstream impact cases. At time $t = 1{\cdot}0$ s (Fig. 5(a)), grains overflow onto the channel bed.

In the physical tests, the flow front cascades over the barrier in a wide arc. By contrast, in the continuum model, material overflows down onto the channel in a narrow, well-defined curve. The difference in spreading during overflow can be attributed to the discrete nature of the physical sand flow: binary particle collisions tend to promote spreading, but such mechanisms are not captured in the continuum model. Furthermore, the physical overflow pattern may also be influenced by air drag. Hákonardóttir *et al*. (2003a) and Naaim-Bouvet *et al*. (2004) observed that the effect of air in the formation of the granular jet downstream of barriers is broadly negligible, assuming the incoming granular flow is dense, comprising grains of high density based on the experimental evidence of small-scale dry granular flows overflowing an obstacle. Furthermore, Börzsönyi & Ecke (2006) performed flume experiments using dry granular flows with and without a vacuum, demonstrating that air can influence flow kinematics for small particles such as sand. Although the continuum model neither captures binary particle collisions nor considers an air phase, the downstream overflow reach is similar for the observed and computed tests.

At $t = 1{\cdot}2$ s (Fig. 4(b)), the physical granular overflow spreads in front of the upstream barrier at landing. The physical and numerical flows reach the downstream barrier simultaneously. Between the location where flow impacts the channel base and the downstream barrier, the flow re-channelises, thinning out in the process. At time $t = 1{\cdot}4$ s (Fig. 4(c)), the flow attains a minimum thickness, enabling quantification of a distinct Froude number.

The numerical model is not able to capture all physically observed mechanisms, especially those relating to the discrete nature of granular overflow. However, it appears to capture the key macroscopic characteristics of flow–structure interaction, and is thus suitable for parametric investigations.

Effects of multiple-barrier spacing and height

Dry granular flow tends to re-accelerate between successive rows of obstacles placed on a slope due to the influence of gravity (Choi *et al*., 2014a, 2014b). Furthermore, the upstream barrier height strongly influences the overflow trajectory, and hence the subsequent landing of the flow onto the channel bed (Kwan, 2012). Figs 5(a), 5(b) and 5(c) show the effects of varying the upstream barrier height and spacing on the induced peak computed horizontal pressure, computed impact velocity and computed impact thickness, respectively. Three upstream barrier heights were considered, specifically $B/h_0 = 1{\cdot}1$; $B/h_0 = 2{\cdot}0$; $B/h_0 = 2{\cdot}5$.

Figure 6(a) shows the influence of barrier spacing and upstream barrier height on the ratio of impact peak pressure between downstream and upstream barriers (i.e. P_d/P_u), where P_d is the peak pressure at the downstream barrier and P_u is the peak pressure at the upstream barrier. The barrier spacing is normalised by the maximum flow thickness (h_0) of the open-channel control test (test ID: FF), that is 90 mm. The reference spacing for the optimum baffle configuration from Law *et al*. (2015) is shown. A further three reference lines for various barrier heights for the recommended normalised barrier spacing are also shown, wherein overflow is assumed to act as a point mass (Kwan *et al*., 2015).

Computed results for multiple-barrier systems show that, in terms of normalised impact pressure, the optimum normalised barrier spacing (L/h_0) depends on barrier height. The shortest upstream barrier ($B/h_0 = 1{\cdot}1$) produces the highest normalised impact pressure for each barrier spacing. There is a minimum at around $L/h_0 = 9{\cdot}0$. For lower values of L/h_0, the impact pressure is higher because overflow tends to hit the downstream barrier directly, rather than

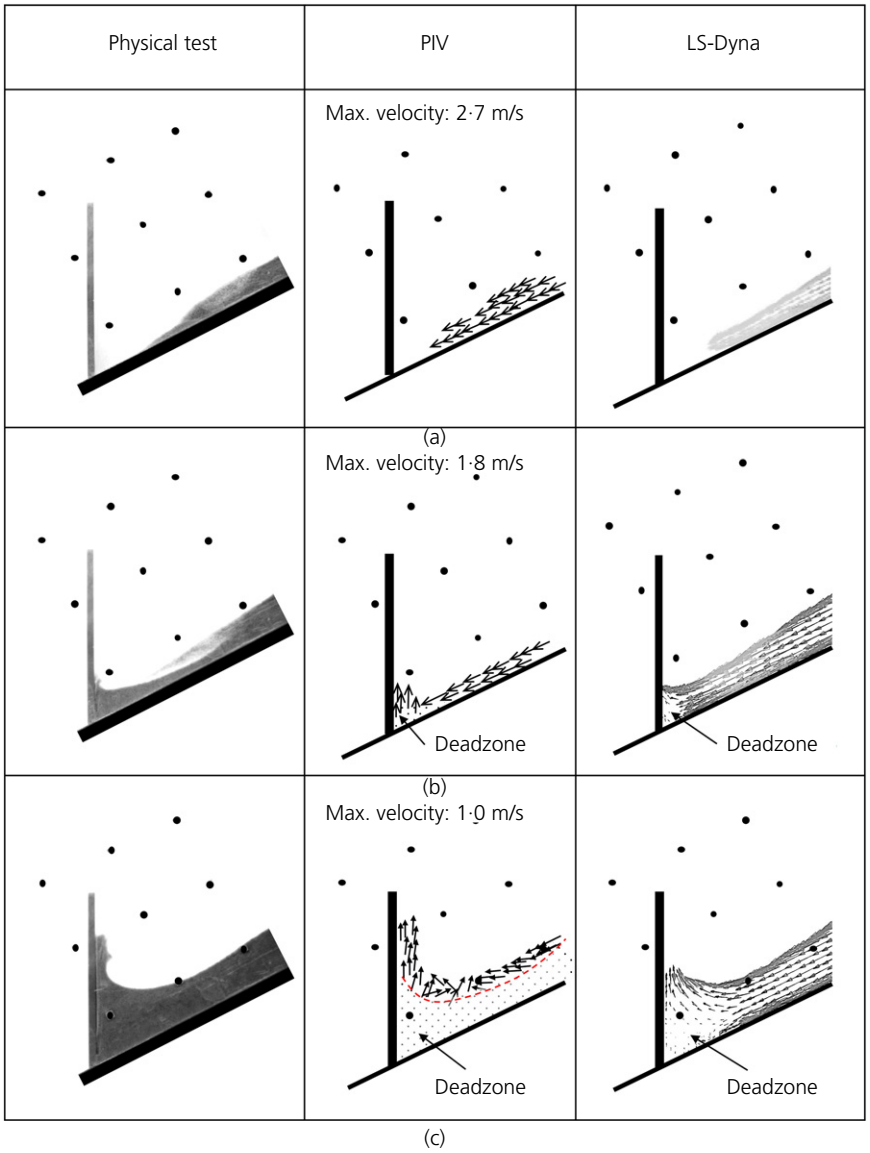

Fig. 4. Comparison of impact kinematics for the first barrier with a normalised height of 2·9 (260 mm): (a) $t = 0{\cdot}15$ s; (b) $t = 0{\cdot}19$ s; (c) $t = 0{\cdot}27$ s (test ID: PX6-B260)

impacting the channel base before impacting the downstream barrier. However, for higher values of L/h_0, overflowing material is able to substantially re-accelerate as it moves downstream, thinning in the process. This tends to increase the pre-impact velocity but reduce the thickness. Competition between these two mechanisms causes the minimum pressure at $L/h_0 = 9{\cdot}0$.

The tallest upstream barrier ($B/h_0 = 2{\cdot}5$) consistently produces intermediate impact pressures (between the other two barrier heights). Similar mechanisms are apparent for the case where $B/h_0 = 1{\cdot}1$. However, for $B/h_0 = 2{\cdot}5$, the minimum value is shifted sharply to the left, lying at around $L/h_0 = 6{\cdot}0$. This is because of variation in material trajectory: for the taller barrier, grains have substantially less downstream momentum when they start to overflow, and so the trajectory tends to be closer to the vertical (consistent with the theoretical approach suggested by Kwan *et al.* (2015)). The shifted minimum pressure is because flow thus tends to impact the channel base further upstream, causing re-acceleration to commence further upstream.

The barrier height of $B/h_0 = 2{\cdot}0$ shows a lower minimum pressure compared to the other two cases. There is a balance between attenuating enough flow energy upon initial impact and preventing an excessive gain in potential energy during overflow. The optimum geometric configuration, specifically a barrier height of $B/h_0 = 2{\cdot}0$ and a normalised barrier spacing of $L/h_0 = 6{\cdot}7$, is double that recommended by the analytical approach of Kwan *et al.* (2015). When the computed flow impacts the channel base, complex energy-dissipation mechanisms occur: the impacting flow loses energy through inelastic collisions, but simultaneously is subject to dynamic confining pressure from flow above. However, the analytical approach recommended by Kwan *et al.* (2015) simplifies the flow as a point mass, ignoring the influence of this confining pressure.

There is a contrast with spacing recommendations for baffles, which must be closely spaced to enable deflection of granular jets onto adjacent baffles and dissipate energy (Choi *et al.*, 2014a), although the goal is not to retain material. Multiple-barrier configuration can nonetheless be streamlined using an appropriate upstream barrier height and barrier spacing.

Effects of upstream flow–barrier interaction to downstream flow velocity and flow-thinning

Figure 6(b) shows the impact velocity on the downstream barrier for different upstream barrier heights. The impact

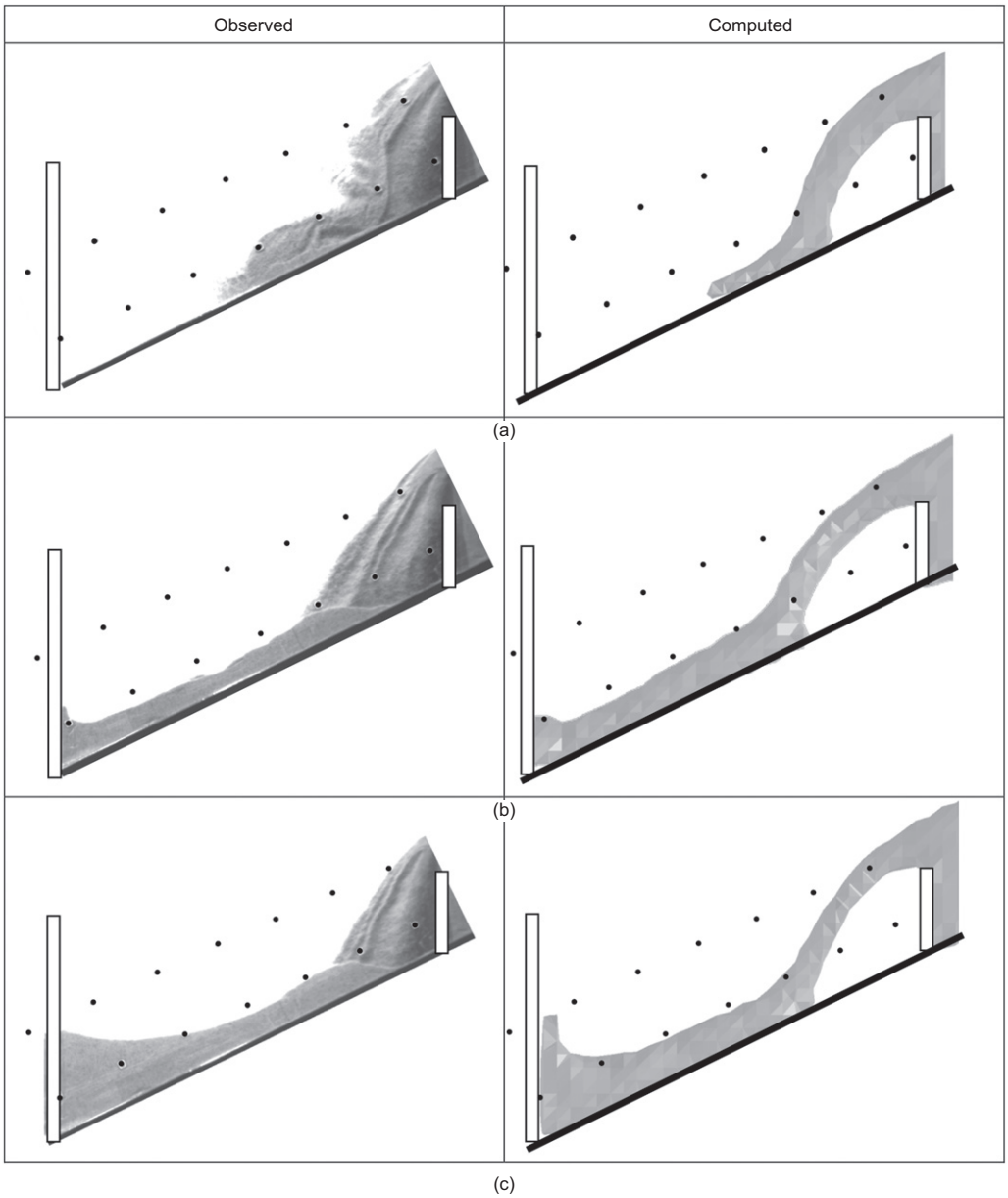

Fig. 5. Comparison of overflow kinematics between barriers: (a) $t = 1{\cdot}0$ s; (b) $t = 1{\cdot}2$ s; (c) $t = 1{\cdot}4$ s after the gate opened (test ID: PX6-B180)

velocity increases with spacing, since the flow re-accelerates along the channel before impacting the downstream barrier (Fig. 6(b)). Shorter barriers ($B/h_0 = 1{\cdot}1$) have the highest impact velocities, as overflowing material retains a substantial amount of momentum in the downstream direction. By increasing the upstream barrier height from $B/h_0 = 1{\cdot}1$ to $B/h_0 = 2{\cdot}0$, a noticeable reduction in horizontal impact velocity is observed. The lower impact horizontal velocity is attributed to more energy attenuated from the taller upstream barrier. In contrast, taller barriers ($B/h_0 = 2{\cdot}5$) prolong the impact process. The runup mechanism continues for longer, and prevents the most energetic material from travelling downstream; lower overflow velocities are achieved by way of the transfer of kinetic energy to gravitational potential energy. However, the impact velocity for $B/h_0 = 2{\cdot}5$ is higher than for $B/h_0 = 2{\cdot}0$ due to the lack of frictional resistance during freefall (since the flow touches neither the structure nor the channel), and the increased distance available for re-acceleration. Additionally, the flow trajectory becomes closer to the vertical as the barrier height increases, thus impacting the channel base further upstream. The flow can thus accelerate over a longer distance after hitting the channel base for any given geometric barrier configuration. The optimum upstream barrier height is $B/h_0 = 2{\cdot}0$.

Figure 6(c) shows the effect of upstream barrier height on impact thickness. Taller upstream barriers prolong the impact process and retain more granular flow. This reduces the overflowing discharge, and by extension the re-channelised flow mass, thus causing very thin flows. However, at a normalised barrier spacing of about $L/h_0 = 9$ the impact thickness is no longer governed by the barrier height. This implies that flow characteristics can be ignored for barrier spacing of $L/h_0 > 9$, meaning that purely geometric considerations for volume can be employed, although since flow-thinning occurs lower at velocities, smaller L/h_0 are recommended.

In addition, the impact Froude number as a function of L/h_0 at the downstream barrier is shown in Fig. 6(d). The Froude number is quantified as the ratio between the maximum frontal impact velocity and the square root of the flow depth before impact. The flow velocity and thickness are computed using finite-element simulations based on the conservation of momentum. Fr increases from 2·5 to 4·5 in the range of barrier spacing ratios (L/h_0) from 4·0 to 17·0.

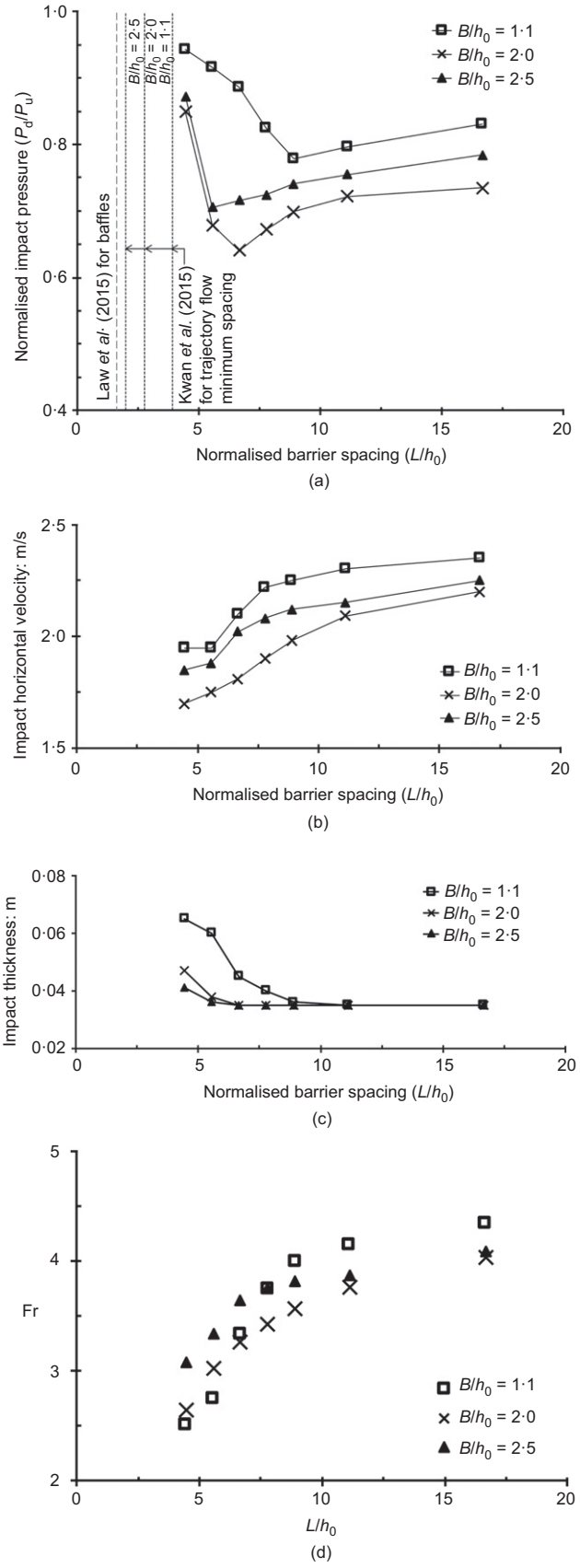

Fig. 6. Influence of barrier height and spacing: (a) maximum impact horizontal pressure ratio between downstream and upstream barriers; (b) impact velocity; (c) impact thickness; (d) Froude number

The Froude conditions are lowest for a B/h_0 ratio of 1·1. This is because the barrier is short, so the flows that develop during landing are thick, and thus the Froude conditions are dominated by flow thickness. However, for this ratio of B/h_0, Fr is higher for larger barrier spacings. This is because the dry sand flow is able to re-accelerate down the channel, and so the Froude conditions become dominated by velocity.

When comparing Figs 6(a) and 6(d), results reveal that there is an increase in scaled impact load downstream from the barrier when the ratio $L/h_0 > 10{\cdot}0$. For this range, the scaled impact load is proportional to Fr; Fr here becomes greater than around 4·0. This is because the Froude conditions are dominated by the velocity component, so the component of lateral scaled impact load due to the self-weight of the flow is negligible (Faug *et al.*, 2009). For Fr less than 4·0, the scaled impact load increases in inverse proportion to the Froude conditions due to the increased importance of the self-weight of the flow (Sovilla *et al.*, 2016).

These findings imply that multiple barriers should not be installed uniformly (Kwan *et al.*, 2015); instead, using taller barriers further upstream can reduce the scale of downstream ones. Furthermore, barriers should not be installed at the point where debris lands; spacing should be further apart to allow flow thinning, thus tending to encourage runup and reduce impact force.

Hydrodynamic impact pressure

The computed pressure is calculated from the reaction of the rigid barrier to the impact of the flow. Interaction between the dry granular material (ALE-based solid elements) and the rigid barrier and channel (shell elements) is modelled using finite-element contacts. The independent motion of the contacting elements is then calculated over a small time step on the order of microseconds. Any penetration of the flow material into the barrier or channel base results in a normal interface reaction force which is distributed evenly to both the flow and the barrier/channel base. The impacting granular material then sustains a reaction force. The magnitude of this force is proportional to the amount of penetration and is determined using an interface spring stiffness governed by the Young's modulus of the flow material and barrier/channel base.

It is noted that there exist several studies on granular flows passing over a barrier that have investigated the force on the barrier, which is affected by the formation of a dead zone. Faug *et al.* (2009) and Chanut *et al.* (2010) have proposed equations for steady and unsteady regimes, respectively. These equations have been tested experimentally using laboratory tests in Faug *et al.* (2011), and an overview and implications for full-scale granular mass movements has been presented in Faug *et al.* (2012).

Figure 7(a) presents a comparison between the impact pressure as calculated by the hydrodynamic equation (equation (3)) and that computed using LS-Dyna. The coefficient α was assumed to be 1·0, as recommended by Jóhannesson *et al.* (2009). The normalised barrier spacing is plotted on the x-axis and the computed pressure normalised by the theoretical pressure is plotted on the y-axis. Three ratios between the barrier height and the flow thickness B/h_0 have been plotted. There is relatively little difference between the three normalised impact pressures, lending confidence to the numerical model. For the smallest normalised barrier spacing considered in this study (around five), the computed pressure is around 50% greater than that obtained from the hydrodynamic equation. This is because the impacting flow is not channelised, violating a fundamental assumption of the hydrodynamic equation. The pressure due to the flow piling up on top of the dead zone, rather than flowing across it, is increased. This is not taken into account in equation (3). For larger barrier spacings, the theoretical impact pressure

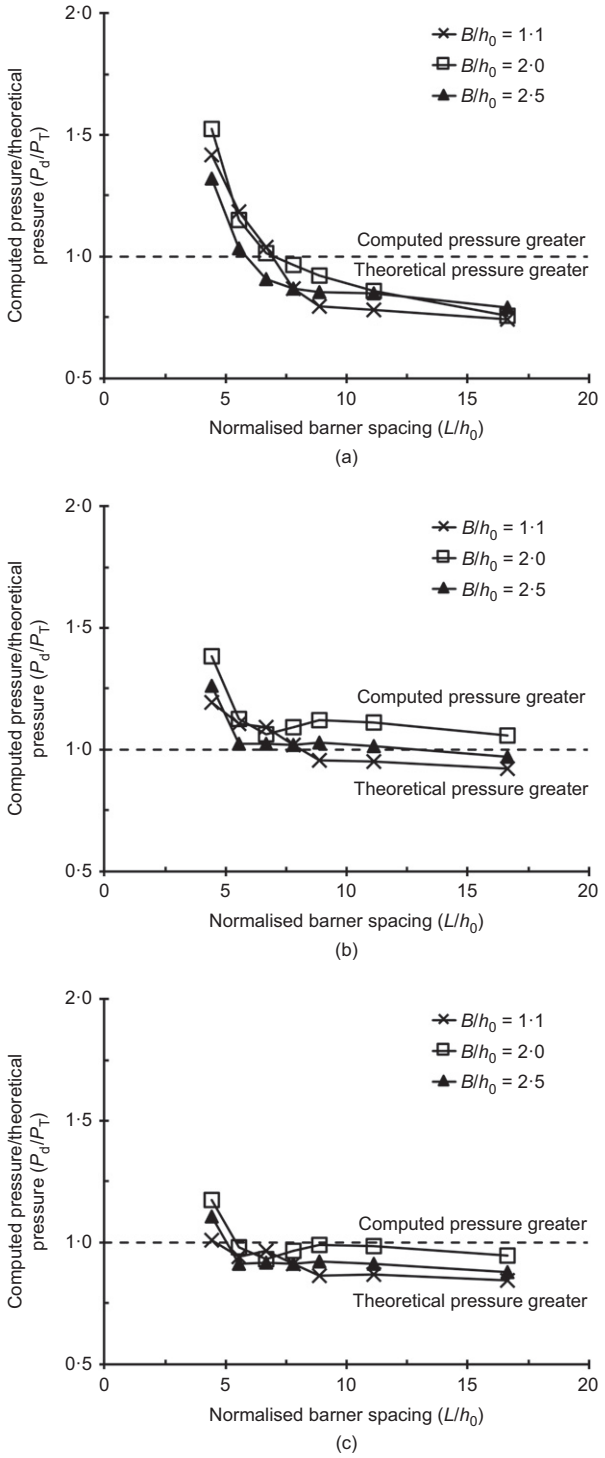

Fig. 7. Comparison of computed pressure with (a) theoretical hydrodynamic pressure ($\alpha = 1{\cdot}0$) and (b) theoretical predictions by Faug *et al.* (2009) and (c) theoretical predictions by Chanut *et al.* (2010) at downstream barrier against normalised barrier spacing

exceeds the computed pressure. By contrast, equation (3) assumes that all the momentum is transferred into the barrier, in the simulations the pressure due to the momentum acting on the barrier is reduced due to runup. Results in Fig. 7(a) show that P_d/P_T is a function of L/h_0, which in turn is a function of the Froude conditions. A constant α value is thus not reasonable to represent the impact load characteristics under different Froude conditions.

For $L/h_0 < 6{\cdot}0$, the computed pressure is higher than the theoretical pressure, whereas for $L/h_0 > 8{\cdot}0$, the reverse is true. Jóhannesson *et al.* (2009) reported that the α value increases with the flow thickness but decreases with flow velocity. This implies that the α value should be larger than 1·0 during the immediate landing zone with larger frontal flow thickness, whereas it should be less than 1·0 further downstream after the velocity has increased.

Figure 7(b) shows a similar comparison between the computed pressure and that computed from the equation presented in Faug *et al.* (2009) (equation (6))

$$F_n = F_{dyn} + F_{pressure} + F_{weight-friction} \tag{6}$$

where F_n is the total normal force exerted on the wall, F_{dyn} is the hydrodynamic force, $F_{pressure}$ is the hydrostatic force and $F_{weight\text{-}friction}$ is a force that is based on the self-weight of the flow volume minus the basal friction. This can be split up into equations (7)–(9)

$$F_{dyn} = \beta\rho u^2 h(1 - \delta_u \cos\alpha_o) \tag{7}$$

$$F_{pressure} = \frac{1}{2} k\rho \boldsymbol{g} u^2 \cos\theta \tag{8}$$

$$F_{weight-friction} = \rho_1 \boldsymbol{g} V(\sin\theta - \mu_{zm}\cos\theta) \tag{9}$$

where β is an acceleration term linked to the velocity profile, and is taken to be 1·0; ρ is density; v is velocity; h is flow thickness; α_o is overflow angle relative to the channel inclination θ; k is the earth pressure coefficient; V is the volume of the zone of influence of the obstacle (volume of the dead zone plus volume of the flowing material above); and μ_{zm} is a steady-state basal friction coefficient which is set as 0·25. δ_u is a dimensionless number and is the velocity of the disturbed flow at the top of the barrier relative to the far-field undisturbed flow (before the zone of influence or dead zone of the barrier). For the calculations in this study, its value was extracted from the numerical finite-element simulations of the runup overflow above the barrier and the undisturbed flow was taken immediately before impacting the dead zone of the barrier.

Again, there is little difference between the three normalised lines plotted, and again, for the smallest normalised barrier spacing, the computed pressure exceeds the theoretical pressure substantially. This is also because the fundamental assumption of the equation is that the flow is channelised, which is not the case for this barrier spacing; furthermore, the equation does not take into account the overburden pressure from the material raining down on top of the impacting flow. For larger barrier spacings, good agreement is seen between computed and theoretical results, demonstrating the validity of equation (9).

Figure 7(c) compares the theoretical equation for impact pressure from Chanut *et al.* (2010), which is the same as equation (9), against that computed from LS-Dyna. The equation has been modified to include a time-varying basal friction coefficient μ^*_{zm} (equation (10))

$$\mu^*_{zm}(t) = c_\mu \tan[\theta - \alpha_{zm}(t)] \tag{10}$$

where c_μ is a calibration parameter depending on the channel inclination and α_{zm} is the dead zone angle. If $c_\mu = 0$, then it is assumed that there is no friction. If $c_\mu = 1$, then the friction becomes a function of the difference between μ^*_{zm} (the slope angle of the chute) and α_{zm} (t) (the dead zone angle made with the inclined bottom). According to Chanut *et al.* (2010), the latter option is more appropriate at steep inclinations (fast flows), whereas the former is more suitable for shallower slopes, close to the friction angle associated with quasi-static deformations. c_μ is set to be zero for this study (Chanut *et al.*, 2010). For the smallest barrier spacing, the computed data

are again larger than the theoretical data, owing to the extra material raining down. The basal resistance is larger than for the equation proposed in Faug *et al*. (2009), so the theoretical prediction is larger for this case than for the computed data.

Impact kinematics

The runup height is an important consideration for the design of barrier height. Figs 8(a) and 8(b) show the runup kinematics of granular flow impacting the upstream ($B = 180$ mm, i.e. $B/h_0 = 2{\cdot}0$) and downstream barriers ($B = 500$ mm), respectively. The measured velocity field directly in front of the barrier is obtained using PIV (White *et al*., 2003). The computed velocity profile is from just in front of the barrier. The resultant is decomposed into horizontal and vertical components; positive vertical velocity denotes an upwards orthogonal direction from the channel base, whereas positive horizontal velocity denotes a slope-parallel upstream direction. Both the momentum and energy approaches are shown, providing a theoretical indication of momentum and energy available before impacting the upstream and downstream barrier. Choi *et al*. (2015) report that dry granular flow runup height h_r is closely captured using the momentum-based approach proposed by Jóhannesson *et al*. (2009). Jóhannesson *et al*. (2009) proposed an analytic solution for calculation of run-up height of a snow avalanche impacting a rigid barrier in a uniform channel, based on the work of Hákonardóttir *et al*. (2003a). The equation is derived based on the conservation of mass and momentum for a shock wave. A back-wave is formed after impacting the rigid barrier. By choosing a reference frame, the travelling speed of the back-wave can be calculated. The runup height is then calculated based on the conservation of remaining mass travelling upward along the barrier and the impact momentum (equation (11))

$$2\mathrm{Fr}^2 + 1 = \frac{\rho_d}{\rho_u}\left(\frac{h_r}{h_u}\right) - \frac{h_r}{h_u} + \left(\frac{\rho_d}{\rho_u}\frac{h_r}{h_u}\right)^{-1} \tag{11}$$

where ρ is the bulk flow density; subscripts 'd' and 'u' indicate 'downstream' and 'upstream', respectively. The computed maximum runup height is broadly comparable to the prediction by Jóhannesson *et al*. (2009).

Koo *et al*. (2017) proposed an analytic solution (equation (12)) for calculation of runup height based on the conservation of energy in the runup process. The runup velocity is estimated by applying a reduction factor to the frontal velocity before impact, which takes into account the reduction in flow velocity due to two distinct effects: (*a*) energy loss due to frictional resistance between the moving and stationary dead zone (not accounted for in equation (11)), and (*b*) conversion from kinetic to potential energy.

$$v_{ru} = v(1 - R_{ru}) \tag{12}$$

where v_{ru} is the runup velocity; v is the pre-runup free-field velocity; and R_{ru} is a lumped factor, given as follows in equation (13)

$$R_{ru} = 1 - \left[1 - \frac{\boldsymbol{g}(\tan\phi L_T + h_{d2})}{v^2}\right]^{1/2} \tag{13}$$

where h_{d2} is the change in elevation; ϕ is the internal friction angle of the debris; and L_T is the travel distance of the debris during runup.

For the first effect, the energy loss can be calculated by determining the work done to overcome the frictional resistance of the oncoming layer of grains, which are travelling over the dead zone. This method assumes that no back wave develops and that the runup density and thickness remains constant. By contrast, the relationship proposed by Jóhannesson *et al*. (2009) in equation (11) assumes conversation of momentum without considering friction loss, as well as the propagation of a granular bore. Both methods assume conservation of mass during the runup processes. However, no inter-grain shearing was considered, causing the predictions to be conservative when compared to the numerical results, as shown in Fig. 7(a), although the maximum runup height is close to the prediction by Jóhannesson *et al*. (2009).

Figure 8(a) also shows a comparison of the measured and computed velocity resultants for the upstream barrier. Flow velocity decreases with barrier height, since kinetic energy is converted into gravitational potential energy through runup and dissipated during dead zone formation. Notably, the vertical component exhibits an abrupt directional trajectory change, which is significant because upwards motion does not induce horizontal loading on the barrier, whereas downward motion tends to lead to momentum transfer into the barrier. This sudden trajectory reversal is due to dead zone formation. Upstream flow material is arrested in sheets on top of the dead zone, facilitating runup (i.e. directional transfer of flow momentum). The reversal of the vertical velocity component occurs between $B/h_0 = 1{\cdot}0$ and $1{\cdot}5$. This implies that there can be potential barrier optimisation by reducing barrier reinforcement above a set

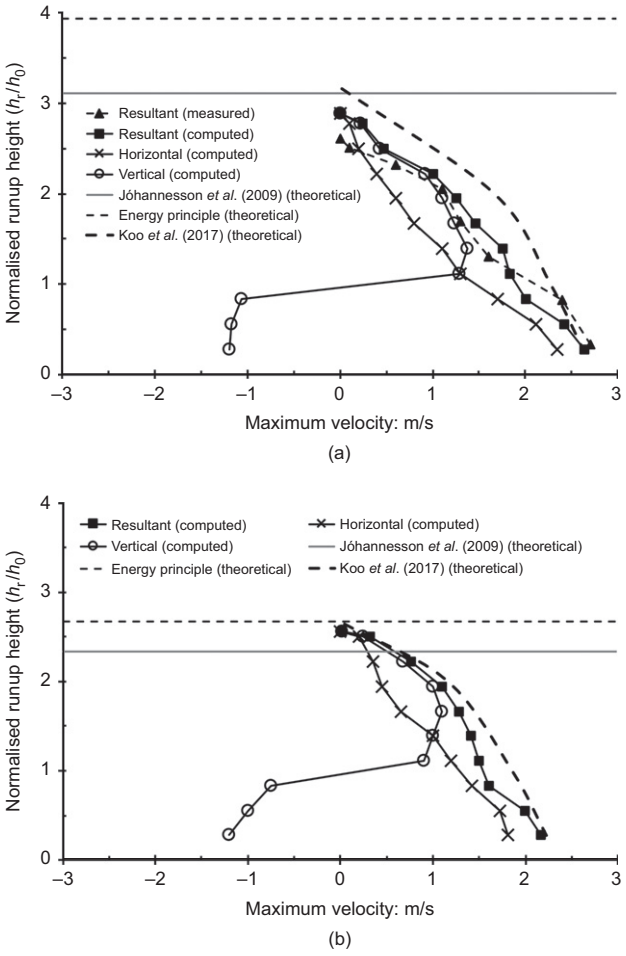

Fig. 8. Comparison of runup kinematics: (a) upstream barrier; (b) downstream barrier with spacing 600 mm for $B/h_0 = 2{\cdot}0$ (negative velocity means downward or upstream flow direction and positive velocity means upward and downstream flow direction)

height. For multiple-barrier systems, dead-zone formation followed by a reversal in the vertical velocity component substantially reduces structural loading away from the base of the barrier.

Figure 8(b) compares the velocity change between the upstream and downstream barriers. The energy principle does not consider varying flow dynamics due to the presence of upstream obstacles, and thus overestimates the energy available for runup by around 25% for the downstream barrier. Although the magnitude of velocity decreases at the downstream barrier, the rate of kinetic energy increase with barrier height does not appear to change significantly due to similar barrier configurations. However, the impact pressure at the downstream barrier is significantly correlated to the remaining momentum of the overflow at the upstream barrier. The runup mechanism at the dead zone dissipates energy effectively, similar to a hydraulic jump, owing to an obstruction placed in the passage of the flow. This implies that the downstream barrier height can safely be reduced.

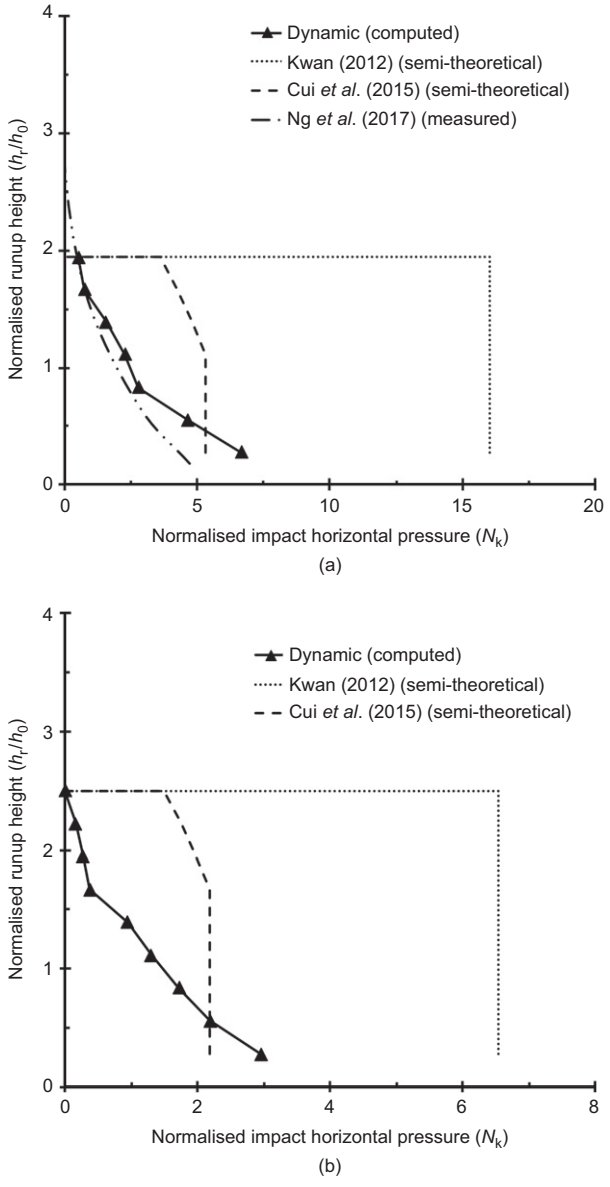

Fig. 9. Comparison of runup and impact dynamics: (a) upstream barrier; (b) downstream barrier with spacing 600 mm ($L/h_0 = 6{\cdot}7$) for $B/h_0 = 2{\cdot}0$

Barrier response

Figures 9(a) and 9(b) show the maximum normalised dynamic impact pressure along the barrier height for the upstream and downstream barriers, respectively. The impact pressure is normalised by the maximum theoretical static pressure at rest by a k_0 value (Jaky, 1944) (i.e. $N_k = P_d/P_s$ where P_s is the maximum static pressure acting at the base of the barrier and $P_s = k_0 \rho \boldsymbol{g} h_{max}$). The theoretical k_0 value is equal to $1 - \sin \phi$ at the rest condition. The computed loading profiles from this study are compared with the hydrodynamic equation, using the α values proposed by Cui *et al*. (2015) and Kwan (2012). Cui *et al*. (2015) empirically recommend the peak pressure at the top to be 0·68 times the peak pressure at the base of the barrier, whereas Kwan (2012) conservatively assumes a constant impact pressure along the height of the barrier, equal to the maximum pressure at the base. Finally, directly measured results for dry granular flows impacting an orthogonal rigid barrier from centrifuge tests (Ng *et al*., 2017) with similar impact Froude conditions (Fr = 3·5, the same as for this study) are shown.

The computed dynamic load for the upstream barrier (Fig. 8(a)) is largest at the base and rapidly diminishes along the upper half of the barrier, due to rapid directional transfer of flow momentum after impact. The material at the base of the vertical barrier cannot easily run up because of geometric constraints, and may be subject to high confining stress, increasing the horizontal pressure.

The hydrodynamic model over-predicts the horizontal pressure at the base of the barrier when using a constant α value of 2·5, as recommended by Kwan (2012), because flow momentum redirection through the runup mechanism is neglected. By contrast, the α value calculated using the relationship proposed by Cui *et al*. (2015) is 0·8, predicting pressure on the lower half of the barrier well, but over-estimating it nearer the top. The proposed impact pressure profile by Cui *et al*. (2015) was based on load measurements on a steel column with a B/h_0 ratio less than 1·5. Low runup heights were recorded as flow could spread around the obstacle, limiting runup – a fundamental difference from the results presented in this study.

The measured dynamic loads in centrifuge tests for granular flow by Ng *et al*. (2017) show lower pressure near the base but higher pressure near the top. The lower pressure at the base can be attributed to the orthogonal barrier configuration, with greater potential for runup than in the present study, where the angle between barrier and channel base is smaller, tending to subject material at the base of the barrier to higher confining pressure. For an orthogonal barrier, runup is higher and thicker (Choi *et al*., 2015) and so the horizontal pressure is higher nearer the very top than for the computed results in this study. The numerical results show that there is little chance of overturning failure for a B/h_0 ratio of at least 2·0, since most of the loading is at the base, meaning that requirements for bending moment reinforcement at the barrier base can be safely reduced.

Figure 9(b) shows impact pressure on the downstream barrier. There is a substantial reduction in horizontal pressure compared to the upstream barrier for the optimised spacing ratio L/h_0 of 7·0. This is due to the reduced flow volume, velocity and thickness impacting the downstream barrier. This is consistent with Ashwood & Hungr (2016), who reported that thinner flow fronts encouraged runup, thus inducing less impact pressure. The predicted maximum pressure from the conventional hydrodynamic equation (Kwan, 2012) is substantially larger than the computed results, since runup or overflow interaction mechanisms in multiple-barrier systems are not considered. In contrast, Cui *et al*. (2015) consider the change of Fr at the downstream

barrier for impact, producing a closer match with the numerical results (within 50%).

The mechanisms of runup at the upstream barrier and flow thinning between the two successive barriers have profound effects on dynamic impact pressures at the downstream barrier. Considering the effects of the upstream barrier on downstream Froude conditions can facilitate streamlined design of downstream barriers for design impact load, but not for retention capacity.

SUMMARY AND CONCLUSIONS

A series of physical flume tests were conducted to study the interaction of dry sand flow with a dual-barrier system. Three-dimensional numerical back-analysis and a parametric study investigating the effects of barrier height and spacing between barriers were then performed using LS-Dyna. It should be noted that, although dry sand constitutes a simple and repeatable medium for understanding fundamental interaction mechanisms between flows and multiple barriers, it is unable to capture flow effects due to the presence of a viscous liquid. Results are therefore not directly applicable to the mitigation of debris flows, although they provide a useful benchmark. This notwithstanding, key results are summarised as follows.

(*a*) There are two key mechanisms that are not considered by existing design approaches that alter downstream flow within a dual-barrier system: (i) flow momentum redirection through the runup mechanism at the upstream barrier, reducing pre-impact momentum at the downstream barrier; and (ii) downstream flow-thinning. Runup mechanisms at the upstream barrier and flow-thinning between the two barriers profoundly affect dynamic impact pressures at the downstream barrier. Proper installation of multiple-barrier systems can avoid unnecessarily large dynamic impact pressures at the downstream barrier.

(*b*) By adopting an optimised barrier spacing ratio L/h_0 of 7·0, the downstream design barrier height and impact pressure can be reduced by 17% and 35%, respectively. These imply that design reinforcements for downstream barriers can be reduced.

(*c*) The optimum configuration entails a normalised barrier height of $B/h_0 = 2{\cdot}0$. The upstream barrier height should be larger than two times the maximum flow thickness to dissipate energy effectively by flow momentum redirection (i.e. runup).

(*d*) Impact pressures at the downstream barrier may be underestimated by up to 50% at a barrier spacing of $L/h_0 < 6$, and overestimated at a barrier spacing of $L/h_0 > 6$ by up to 30%, if a hydrodynamic pressure coefficient of unity is adopted. This implies that adopting a constant pressure coefficient is inappropriate for multiple-barrier system design.

ACKNOWLEDGEMENTS

The authors are grateful for financial support from research grant T22-603/15N provided by the Research Grants Council of the Hong Kong SAR Government, China. This paper is published with the permission of the Head of the Geotechnical Engineering Office and the Director of Civil Engineering and Development, the Hong Kong SAR Government, China. The authors would like to thank the HKUST Jockey Club Institute for Advanced Research for their support.

NOTATION

B	barrier height
B_d	barrier height downstream
B_u	barrier height upstream
c_μ	calibration parameter
E	Young's modulus
F_{dyn}	hydrodynamic force
F_n	total normal force exerted on the wall
$F_{pressure}$	hydrostatic force
Fr	Froude number
$F_{weight\text{-}friction}$	force considering self-weight of flow and basal friction
G	shear modulus
$\boldsymbol{g}$	acceleration due to gravity
h	flow thickness
h_{d2}	change in elevation
h_0	open channel flow thickness (i.e. without barrier)
h_r	runup height (i.e. with barrier)
k_0	static earth pressure coefficient
L	barrier spacing
L_T	travel distance of the debris during runup
N	normal force
N_k	normalised impact pressure to k_0
$\boldsymbol{n}$	unit vector
P_d	computed maximum computed impact pressure at downstream barrier
P_s	maximum static pressure acting at base of barrier
P_T	theoretical maximum impact pressure
P_u	computed maximum impact pressure at upstream barrier
R_{ru}	lumped correction factor
S	interface shear resistance
$\boldsymbol{T}$	stress vector
t	time
V	bulk volume of flow
v	flow velocity
v_{ru}	runup velococity
x_i	overflow length
$\ddot{x}$	acceleration
α	empirical dynamic correction coefficient
α_o	overflow velocity relative to slope angle
α_{zm}	deadzone angle
β	acceleration term linked to the velocity profile
δ_u	mean approaching flow velocity
θ	channel inclination
μ_{zm}	steady-state basal friction coefficient
μ^*_{zm}	unsteady-state basal friction coefficient
ν	Poisson modulus
ρ	bulk flow density
ρ_d	bulk flow density downstream
ρ_m	material density
ρ_u	bulk flow density upstream
$\boldsymbol{\sigma}_{ij}$	Cauchy stress tensor
ϕ	internal friction of sand
ϕ_b	basal (interface) friction angle

REFERENCES

Armanini, A. (2015). Closure relations for mobile bed flows in a wide range of slopes and concentrations. *Adv. Water Resources* **81**, 75–83, https://doi.org/10.1016/j.advwatres.2014.11.003.

Armanini, A., Larcher, M. & Odorizzi, M. (2011). Dynamic impact of a debris flow front against a vertical wall. *Proceedings of the 5th international conference on debris-flow hazards "mitigation, mechanics, prediction and assessment"*, Padua, Italy, pp. 1041–1049.

Armanini, A., Larcher, M., Nucci, E. & Dumbser, M. (2014). Submerged granular channel flows driven by gravity. *Adv. Water Resources* **63**, 1–10, https://doi.org/10.1016/j.advwatres.2013.10.007.

Ashwood, W. & Hungr, O. (2016). Estimating the total resisting force in a flexible barrier impacted by a granular avalanche using physical and numerical modelling. *Can. Geotech. J.* **53**, No. 10, 1700–1717.

Bazilevs, Y., Calo, V. M., Hughes, T. J. R. & Zhang, Y. (2008). Isogeometric fluid–structure interaction: theory, algorithms, and computations. *Comput. Mech.* **43**, No. 1, 3–37.

Börzsönyi, T. & Ecke, R. E. (2006). Rapid granular flows on a rough incline: phase diagram, gas transition, and effects of air drag. *Phys. Rev. E* **74**, No. 6, 061301.

Bryant, S. K., Take, W. A., Bowman, E. T. & Millen, M. D. L. (2015). Physical and numerical modelling of dry granular flows under Coriolis conditions. *Géotechnique* **65**, No. 3, 188–200, http://dx.doi.org/10.1680/geot.13.P.208.

CGS (China Geological Survey) (2004). *Design code for debris flow disaster mitigation measures (DZ/T0239-2004)*. Beijing, China: CGS (in Chinese).

Chanut, B., Faug, T. & Naaim, M. (2010). Time-varying force from dense granular avalanches on a wall. *Phys. Rev. E* **82**, No. 4, 041302.

Choi, C. E., Ng, C. W. W., Song, D., Kwan, J. S. H., Shiu, H. Y. K., Ho, K. K. S. & Koo, R. C. H. (2014a). Flume investigation of landslide debris-resisting baffles. *Can. Geotech. J.* **51**, No. 5, 540–553.

Choi, C. E., Ng, C. W. W., Song, D., Law, R. P. H., Kwan, J. S. H. & Ho, K. K. S. (2014b). A computational investigation of baffle configuration on the impedance of channelized debris flow. *Can. Geotech. J.* **52**, No. 2, 182–197.

Choi, C. E., Au-Yeung, S., Ng, C. W. W. & Song, D. (2015). Flume investigation of landslide granular debris and water runup mechanisms. *Géotechnique Lett.* **5**, No. 1, 28–32.

Crosta, G. B., Imposimato, S. & Roddeman, D. G. (2003). Numerical modelling of large landslides stability and runout. *Nat. Hazards Earth Syst. Sci.* **3**, No. 6, 523–538.

Cui, P., Zeng, C. & Lei, Y. (2015). Experimental analysis on the impact force of viscous debris flow. *Earth Surface Process and Landforms* **40**, No. 12, 1644–1655.

Drucker, D. C. & Prager, W. (1952). Soil mechanics and plastic analysis for limit design. *Q. Appl. Math.* **10**, No. 2, 157–165.

Faug, T. (2015a). Depth-averaged analytic solutions for free-surface granular flows impacting rigid walls down inclines. *Phys. Rev. E* **92**, No. 6, 062310.

Faug, T. (2015b). Macroscopic force experienced by extended objects in granular flows over a very broad Froude-number range. *Eur. Phys. J. E* **38**, No. 5, article 34.

Faug, T., Lachamp, P. & Naaim, M. (2002). Experimental investigation on steady granular flows interacting with an obstacle down an inclined channel: study of the dead-zone upstream from the obstacle. Application to interaction between dense snow avalanches and defence structures. *Nat. Hazards Earth Syst. Sci.* **2**, No. 3/4, 187–191.

Faug, T., Naaim, M., Bertrand, D., Lachamp, P. & Naaim-Bouvet, F. (2003). Varying dam height to shorten the run-out of dense avalanche flows: developing a scaling law from laboratory experiments. *Surveys Geophys.* **24**, No. 5–6, 555–568.

Faug, T., Naaim, M. & Naaim-Bouvet, F. (2004). An equation for spreading length, center of mass and maximum run-out shortenings of dense avalanche flows by vertical obstacles. *Cold Regions Sci. Technol.* **39**, No. 2–3, 141–151.

Faug, T., Gauer, P., Lied, K. & Naaim, M. (2008). Overrun length of avalanches overtopping catching dams: cross-comparison of small-scale laboratory experiments and observations from full-scale avalanches. *J. Geophys. Res. Earth Surface* **113**, No. F3, F03009.

Faug, T., Beguin, R. & Chanut, B. (2009). Mean steady granular force on a wall overflowed by free-surface gravity-driven dense flows. *Phys. Rev. E* **80**, No. 2, 021305.

Faug, T., Caccamo, P. & Chanut, B. (2011). Equation for the force experienced by a wall overflowed by a granular avalanche: experimental verification. *Phys. Rev. E* **84**, No. 5, 051301.

Faug, T., Caccamo, P. & Chanut, B. (2012). A scaling law for impact force of a granular avalanche flowing past a wall. *Geophys. Res. Lett.* **39**, No. 23, L23401.

Faug, T., Childs, P., Wyburn, E. & Einav, I. (2015). Standing jumps in shallow granular flows down smooth inclines. *Phys. Fluids* **27**, No. 7, 073304.

Forterre, Y. & Pouliquen, O. (2008). Flows of dense granular media. *Annual Rev. Fluid Mech.* **40**, 1–24, http://dx.doi.org/10.1146/annurev.fluid.40.111406.102142.

Gauer, P., Issler, D., Lied, K., Kristensen, K. Iwe, H., Lied, E., Rammer, L. & Schreiber, H. (2007a). On full-scale avalanche measurements at the Ryggfonn test site, Norway. *Cold Regions Sci. Technol.* **49**, No. 1, 39–53.

Gauer, P., Kern, M., Kirstensen, K., Lied, K. Rammer, L. & Schreiber, H. (2007b). On pulsed Doppler radar measurements of avalanches and their implication to avalanche dynamics. *Cold Regions Sci. Technol.* **50**, No. 1–3, 55–71.

GDR MiDi (2004). On dense granular flows. *Eur. Phys. J. E* **14**, No. 4, 341–365.

Glassey, T. (2013). *Hydrology and check dams analysis in the debris flow context of Illgraben torrent*. MAS practical research project, Swiss Federal Institute of Technology Zurich, Zurich, Switzerland.

Gray, J. M. N. T., Tai, Y. C. & Noelle, S. (2003). Shock waves, dead zones and particle-free regions in rapid granular free-surface flows. *J. Fluid Mech.* **491**, 161–181, https://doi.org/10.1017/S0022112003005317.

Hákonardóttir, K. M., Hogg, A. J., Batey, J. & Wood, A. W. (2003a). Flying avalanches. *Geophys. Res. Lett.* **30**, No. 23, 2191.

Hákonardóttir, K. M., Hogg, A. J., Jóhannesson, T. & Tómasson, G. G. (2003b). A laboratory study of the retarding effects of braking mounds on snow avalanches. *J. Glaciol.* **49**, No. 165, 191–200.

Hallquist, J. O. (2006). *LS-DYNA theory manual*. Livermore, CA, USA: Livermore Software Technology Corporation.

Hübl, J., Suda, J., Proske, D., Kaitna, R. & Scheidl, C. (2009). Debris flow impact estimation. In *Proceedings of international symposium on water management and hydraulic engineering* (ed. C. Popovska), pp. 137–148. Skopje, Macedonia: Ss Cyril and Methodius University.

Hungr, O. & Morgenstern, N. R. (1984). Experiments on the flow behaviour of granular materials at high velocity in an open channel. *Géotechnique* **34**, No. 3, 405–413, http://dx.doi.org/10.1680/geot.1984.34.3.405.

Iverson, R. M. (1997). The physics of debris flows. *Rev. Geophys.* **35**, No. 3, 245–296.

Iverson, R. M. (2015). Scaling and design of landslide and debris-flow experiments. *Geomorphology* **244**, 9–20, https://doi.org/10.1016/j.geomorph.2015.02.033.

Jaky, J. (1944). The coefficient of earth pressure at rest. *J. Soc. Hungarian Archit. Engrs* **78**, No. 22, 355–358.

Jóhannesson, T., Gauer, P., Issler, D. & Lied, K. (2009). *The design of avalanche protection dams: recent practical and theoretical developments*. Brussels, Belgium: European Commission.

Jop, P., Forterre, Y. & Pouliquen, O. (2006). A constitutive law for dense granular flows. *Nature* **441**, No. 7094, 727–730.

Koo, R. C. H., Kwan, J. S. H., Ng, C. W. W., Lam, C., Choi, C. E., Song, D. & Pun, W. K. (2017). Velocity attenuation of debris flows and a new momentum-based load model for rigid barriers. *Landslides* **14**, No. 2, 617–629.

Kwan, J. S. H. (2012). *Supplementary technical guidance on design of rigid debris-resisting barriers, Technical Note No. TN 2/2012*. Hong Kong, China: Geotechnical Engineering Office, Civil Engineering and Development Department, The HKSAR Government.

Kwan, J. S. H., Koo, R. C. H. & Ng, C. W. W. (2015). Landslide mobility analysis for design of multiple debris-resisting barriers. *Can. Geotech. J.* **52**, No. 9, 1345–1359.

Law, R. P. H., Choi, C. E. & Ng, C. W. W. (2015). Discrete element investigation of the influence of debris flow baffles on rigid barrier impact. *Can. Geotech. J.* **53**, No. 2, 179–185.

Mancarella, D. & Hungr, O. (2010). Analysis of runup of granular avalanches against steep, adverse slopes and protective barriers. *Can. Geotech. J.* **47**, No. 8, 827–841.

Naaim, M., Faug, T., Naaim-Bouvet, F. & Eckert, N. (2010). Return period calculation and passive structure design at the Taconnaz avalanche path, France. *Ann. Glaciol.* **51**, No. 54, 89–97.

Naaim-Bouvet, F., Naaim, M. & Faug, T. (2004). Dense and powder avalanches: momentum reduction generated by a dam. *Ann. Glaciol.* **38**, 373–378.

Ng, C. W. W., Choi, C. E., Song, D., Kwan, J. S. H., Shiu, H. Y. K., Ho, K. K. S. & Koo, R. C. H. (2014). Physical modelling of baffles influence on landslide debris mobility. *Landslides* **12**, No. 1, 1–18.

Ng, C. W. W., Song, D., Choi, C. E., Kwan, J. S. H., Shiu, H. Y. K. & Koo, R. C. H. (2017). Centrifuge modelling of dry granular and viscous impact on rigid and flexible barriers. *Can. Geotech. J.* **54**, No. 2, 188–206.

NILIM (National Institute for Land and Infrastructure Management) (2007). *Manual of technical standard for establishing Sabo master plan for debris flow and driftwood, Technical Note of NILIM No. 364*. Tsukuba, Japan: National Institute for Land and Infrastructure Management, Ministry of Land, Infrastructure and Transport (in Japanese).

Olovsson, L. & Souli, M. (2000). ALE and fluid–structure interaction capabilities in LS-DYNA. *Proceedings of the 6th international LS-DYNA conference*, Detroit, MI, USA, vol. 15, pp. 37–46.

Pouliquen, O. (1999). Scaling laws in granular flows down rough inclined planes. *Physics of Fluids* **11**, No. 3, 542–548.

Pudasaini, S. P. & Hutter, K. (2007). *Avalanche dynamics: dynamics of rapid flows of dense granular avalanches*. New York, NY, USA: Springer.

Shum, L. K. W. & Lam, A. Y. T. (2011). *Review of natural terrain landslide risk management practice and mitigation measures, Technical Note TN 3/2011*. Hong Kong, China: Geotechnical Engineering Office, Civil Engineering and Development Department, The HKSAR Government.

Sovilla, B., Faun, T., Köhler, A., Baroudi, D., Fischer, J. T. & Thibert, E. (2016). Gravitational wet avalanche pressure on pylon-like structures. *Cold Regions Sci. Technol.* **126**, 66–75, https://doi.org/10.1016/j.coldregions.2016.03.002.

Thibert, E., Bellot, H., Ravanat, X., Ousset, F., Pulfer, G., Naaim, M., Naaim-bouvet, F., Nishimura, K., Ito, Y., Baroudi, D., Prokop, A., Schon, P., Soruco, A., Vincent, C., Limam, A. & Pesaresi, D. (2013). The full-scale avalanche test site, Lautaret, France. *Proceedings of the international snow science workshop*, Grenoble and Chamonix Mont-Blanc, France, pp. 1358–1365.

Wang, G. L. (2013). Lessons learned from protective measures associated with the 2010 Zhouqu debris flow disaster in China. *Nat. Hazards* **69**, No. 3, 1835–1847.

White, D. J., Take, W. A. & Bolton, M. D. (2003). Soil deformation measurement using particle image velocimetry (PIV) and photogrammetry. *Géotechnique* **53**, No. 7, 619–631, http://dx.doi.org/10.1680/geot.2003.53.7.619.

Wong, H. N. (2009). Rising to the challenges of natural terrain landslides. In *Proceedings of the HKIE geotechnical division annual seminar 2009*, pp. 15–53. Hong Kong, China: Geotechnical Division, The Hong Kong Institution of Engineers.

WSL (Swiss Federal Institute for Snow and Avalanche Research) (2008). *Integral risk management of extremely rapid mass movements*. Birmensdorf, Switzerland: WSL. See http://irasmos.slf.ch/ (accessed 01/08/2017).

Zhou, G. D., Wright, N. G., Sun, Q. C. & Cai, Q. P. (2016). Experimental study on the mobility of channelized granular mass flow. *Acta Geologica Sinica* **90**, No. 3, 801–840.